Nano Research

ISSN 1998-0124 CN 11-5974/O4
https://doi.org/10.1007/s12274-021-3907-9

Research Article

Direct drop-casting synthesis of all-inorganic lead and lead-free halide perovskite microcrystals for high-performance photodetectors

Zhengxun Lai[1], You Meng[1], Fei Wang[1,2,3], Xiuming Bu[1], Wei Wang[1,3], Pengshan Xie[1], Weijun Wang[1], Chuntai Liu[4], SenPo Yip[1,5], and Johnny C. Ho[1,3,5] (✉)

[1] *Department of Materials Science and Engineering, City University of Hong Kong, Kowloon, Hong Kong 999077, China*
[2] *State Key Laboratory of Luminescence and Applications, Changchun Institute of Optics, Fine Mechanics and Physics, Chinese Academy of Sciences, Changchun 130021, China*
[3] *State Key Laboratory of Terahertz and Millimeter Waves, City University of Hong Kong, Kowloon, Hong Kong 999077, China*
[4] *Key Laboratory of Advanced Materials Processing & Mold (Zhengzhou University), Ministry of Education, Zhengzhou 450002, China*
[5] *Institute for Materials Chemistry and Engineering, Kyushu University, Fukuoka 816–8580, Japan*

Received: 28 July 2021 / **Revised:** 15 September 2021 / **Accepted:** 26 September 2021

ABSTRACT

Due to the exciting photoelectric properties, better stability, and environmental-friendly nature, all-inorganic halide perovskites (AIHPs), especially the lead-free perovskites, have attracted worldwide attention. However, the film quality of AIHPs fabricated by typical spin-coating and subsequent high-temperature annealing is still not satisfactory, restricting their further development. Herein, we demonstrate a simple low-temperature solution-processed drop-casting method to achieve highly-crystalline cubic $CsPbBr_3$ and lead-free layer-structured $Cs_3Sb_2I_9$ microcrystals (MCs). This drop-casting technique not only consumes the less amount of precursor solution but also eliminates the high-temperature annealing as compared with those of spin coating. When these MCs are configured into photodetectors, they exhibit superior device performance, which is in distinct contrast to the one of spin-coated counterparts. Specifically, the responsivity of $CsPbBr_3$ MCs is found to be as large as 8,990 mA/W, being 13 times larger than the spin-coated films and even better than many state-of-the-art solution-processed AIHPs devices. This device performance enhancement is attributed to the better film quality and phase purity obtained by the drop-casting method. All these results can evidently fill the "technology gap" for further enhancing the material quality of solution-processed AIHPs and breaking down the barriers that hinder the development of AIHPs based optoelectronic devices.

KEYWORDS

halide perovskite, drop-casting, photodetector, $CsPbBr_3$, $Cs_3Sb_2I_9$

1 Introduction

In recent years, due to the exciting photoelectric properties, organic-inorganic halide perovskites (OIHPs) have attracted worldwide attention. They have been widely explored as active materials for various kinds of optoelectronic devices, including solar cells, photodetectors, and light emitting diodes (LEDs), with significant progress achieved across all the communities [1–9]. However, the stability of OIHPs in the ambient environment is fairly poor, which greatly hinders their practical utilization [10–13]. In this case, the all-inorganic halide perovskites (AIHPs), mainly $CsPbX_3$ (X = I, Br, or Cl), are promising alternatives because of their superior thermal and moisture stability. Unfortunately, for $CsPbI_3$, the black phase of α-$CsPbI_3$ is merely preferred for optoelectronic devices, but it can spontaneously transform to the undesired yellow phase of δ-$CsPbI_3$ with poor optical and electrical properties in the atmosphere of room temperature owing to the phase instability [14, 15]. For $CsPbCl_3$, since its bandgap is about 3.04 eV, this material is mostly employed for the ultraviolet light-related applications rather than the ones involving the visible light. Hence $CsPbBr_3$ is the most appropriate material here for the visible light-related use, particularly for photodetection, where it has good phase and thermal stability.

At the moment, the solution synthesis of high-quality AIHPs is still very challenging, especially the obtained photoelectric performance of solution-processed $CsPbBr_3$ is not satisfactory. The main reasons can be the poor solubility and the complicated phase diagrams of Cs-Pb-X [16, 17]. Besides, the required annealing temperatures of AIHPs fabricated by conventional spin-coating methods are relatively high (about 200–350 °C), which also limits their applications. For example, the high annealing temperatures may decompose other device layers during the fabrication of solar cells or LEDs [18]. Zeng et al. fabricated the $CsPbBr_3$ films by a solution-based space-confine method to overcome the film-forming problem caused by the low solubility of $CsPbBr_3$ [19]. Huang et al. enhanced the concentration of the precursor solution of $CsPbBr_3$ by introducing CsAc and MAAc into the precursor solution system, which can

Address correspondence to johnnyho@cityu.edu.hk

help fabricate high-quality all-inorganic films [20]. Zhang et al. introduced organic n-butylammonium iodide to the AIHP of $CsPbIBr_2$ to decrease the annealing temperatures, but the organic additive would suffer from its stability problem [18]. Although many methods have been used to tackle the drawbacks of conventional solution processing schemes, a simple way to construct the high-quality $CsPbBr_3$ with low temperatures is still in urgent need.

Apart from the lead-based AIHPs mentioned above, the non-toxic lead-free AIHPs are even the more attractive candidates for high-performance optoelectronic devices [21, 22]. These lead-free materials are environmentally friendly and highly desirable for large-scale applications. In the same group as Pb, Sn is usually proposed to replace the Pb constituent in AIHPs. Nevertheless, the Sn^{2+} in $CsSnX_3$ can easily be oxidized to Sn^{4+} irreversibly in ambient air, which deteriorates the material properties [23, 24]. Besides, Bi and Sb can also substitute for the Pb constituent in halide perovskites forming the vacancy-ordered perovskite structure of $A_3B_2X_9$ (A = Cs^+ or MA^+, B = Bi^{3+} or Sb^{3+}). For the Bi-based perovskites, they usually have relatively large bandgaps and a significant amount of defect states, limiting their applications [25]. This way, the Sb-based halide perovskites have drawn all the recent focus. For instance, Zheng et al. fabricated the $Cs_3Sb_2Br_9$ nanoflakes by an inverse temperatures crystallization method, where both the optical and electrical properties were characterized [26]. Szklarz et al. fabricated the $(NH_2CHNH_2)_3Sb_2I_9$ single crystals by slow evaporation of its saturated solution, while their ferroelectricity was studied in detail [27]. Furthermore, there are two identified polymorphs for $Cs_3Sb_2I_9$: the zero-dimensional (0D) dimer phase (D-$Cs_3Sb_2I_9$) that has isolated bi-octahedral $Sb_2I_3^{9-}$ anions and the layered phase (L-$Cs_3Sb_2I_9$) with two-dimensional (2D) corrugated layers, as shown in Figs. 1(a) and 1(b) [28–30]. On the one hand, as D-$Cs_3Sb_2I_9$ has an indirect bandgap of 2.3 eV, it is unfavorable for optoelectronic devices. On the other hand, although L-$Cs_3Sb_2I_9$ has a preferred direct bandgap of 2.08 eV, being ideal for solar cells and photodetectors, the solution synthesis of $Cs_3Sb_2I_9$ would always yield the undesirable phase of D-$Cs_3Sb_2I_9$ rather than the favorable phase of L-$Cs_3Sb_2I_9$, greatly restricting its practical use [28, 29]. In any case, based on these limited studies, the reported material performance is still insufficient for device applications.

In this work, we propose and demonstrate a simple solution processing (i.e., a drop-casting method) method to fabricate high-quality AIHPs of $CsPbBr_3$ and its lead-free counterpart of $Cs_3Sb_2I_9$ microcrystals (MCs) at low temperatures, which can be easily deployed to industry for large-scale production. The $CsPbBr_3$ and $Cs_3Sb_2I_9$ MCs are also configured into photodetectors with detailed evaluation of their photodetection properties and careful comparison against the thin film devices obtained by the conventional spin-coating technique. It is revealed that both the quality and the photodetection performance of the MCs are superior among all the AIHPs films and devices reported in the recent literature. All these results can evidently fill the "technology gap" of how to further enhance the material quality of solution-processed AIHPs and break down the barriers that hinder the development of AIHPs-based optoelectronic devices.

2 Results and discussion

Figure 1(c) depicts the schematic illustration of the drop-casting method developed in this work. To be specific, glass substrates were utilized, being ultrasonically cleaned firstly and treated with oxygen plasma to improve their hydrophilicity. Then 5 μL of $CsPbBr_3$ or $Cs_3Sb_2I_9$ solution was dripped onto the processed substrates. After the solution was spreaded on the substrate, it was

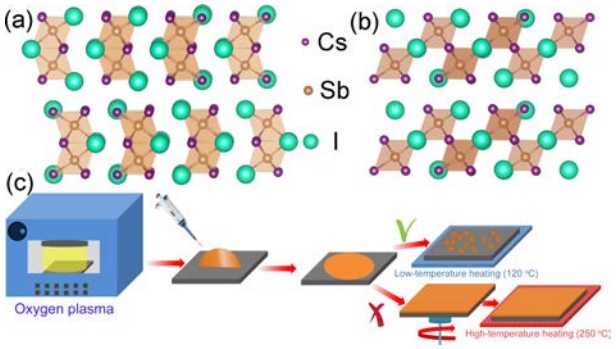

Figure 1 The lattice structure schematics of (a) D-$Cs_3Sb_2I_9$ and (b) L-$Cs_3Sb_2I_9$. (c) The schematic illustration of the drop-casting method and the conventional spin-coating technique.

heated on a hot plate for 5 min, where the temperatures were set at 120 or 70 °C, respectively. The $CsPbBr_3$ or $Cs_3Sb_2I_9$ MCs were then obtained accordingly. Notably, this drop-casting method has obvious advantages over the conventional solution-processed spin-coating technique (Fig. 1(c)). It is notorious that the spin-coating technique requires a relatively large amount of precursor solution to initiate the deposition process, but most of the solution is not consumed and wasted during the process. It also needs a relatively higher temperature for the subsequent annealing process to enhance the film quality. In distinct contrast, this drop-casting method can not only simplify the fabrication procedure by employing a much lower process temperature to attain the better film quality but also minimize the amount of the precursor solution used. All these improvements give a possible plan and direction to improve the insufficiency of the spin-coating method.

After the material deposition, X-ray diffraction (XRD) was performed on the $CsPbBr_3$ MCs, in which the results were compared against the standard XRD pattern of $CsPbBr_3$ (PDF#75–0412, cubic phase, and space group $Pm\bar{3}m$) in Fig. 2(a). It is witnessed that the XRD peaks of the MCs all come from $CsPbBr_3$, suggesting the pure phase of MCs obtained without any other impure phases. Figure 2(b) shows the scanning electron microscope (SEM) image of the MCs, where the large-area SEM image is shown in Fig. S1 in the Electronic Supplementary Material (ESM). We can see that the MCs are regular rectangular shapes with dimensions of ~ 20 μm, which is consistent with the cubic lattice structure of $CsPbBr_3$ [31]. Apart from $CsPbBr_3$ MCs, the structural properties of their lead-free counterpart of $Cs_3Sb_2I_9$ MCs are also thoroughly evaluated. The XRD pattern of the $Cs_3Sb_2I_9$ MCs is shown in Fig. 2(c), in which the pattern can be well fitted with the data from PDF#88–0690 (L-$Cs_3Sb_2I_9$, space group $P\bar{3}m1$). Importantly, there are only obvious peaks of the [001] crystal orientation observed in the XRD pattern, which indicates the preferred stacking direction of the $Cs_3Sb_2I_9$ MCs, further confirming the formation of the desired layered structure of L-$Cs_3Sb_2I_9$ through the drop-casting method. Figure 2(d) shows the SEM image of a typical $Cs_3Sb_2I_9$ MC, where the large-area SEM image is presented in Fig. S2 in the ESM. It is observed that the MCs are regular hexagonal shapes with an edge length of ~ 30 μm that is consistent with the orthorhombic structure of $Cs_3Sb_2I_9$. Besides, as demonstrated in Fig. S2 in the ESM, some relatively small hexagonal MCs are easily stacked on top of the large MCs in a one-by-one manner, yielding the features of flower buds. It is because that the surface of the MCs is the ideal nucleation site of the next MC.

Then the optical properties of the MCs were also studied. The ultraviolet-visible (UV–vis) absorption and photoluminescence (PL) spectra of the MCs are shown in Fig. 3(a). Evidently, the absorption edge is located at 536 nm, from which the bandgap

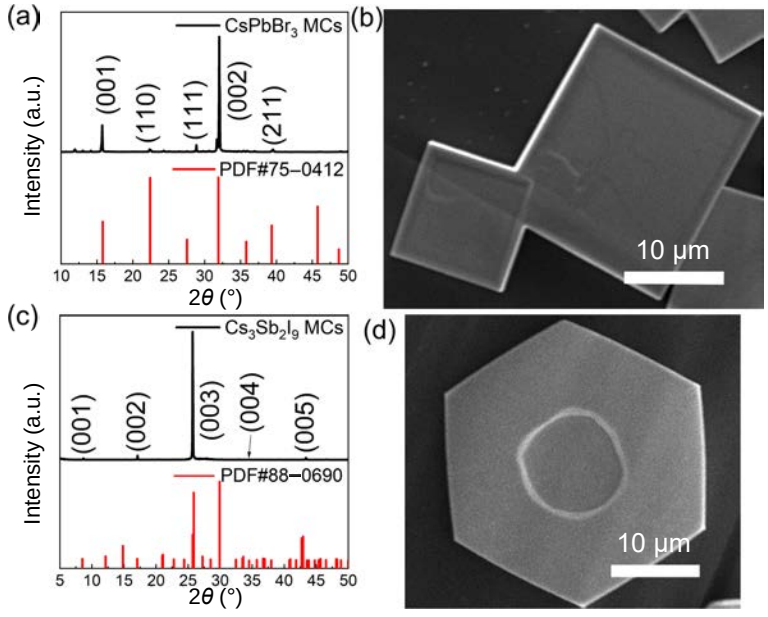

Figure 2 (a) XRD pattern and (b) SEM image of the $CsPbBr_3$ MCs. (c) XRD pattern and (d) SEM image of the $Cs_3Sb_2I_9$ MCs.

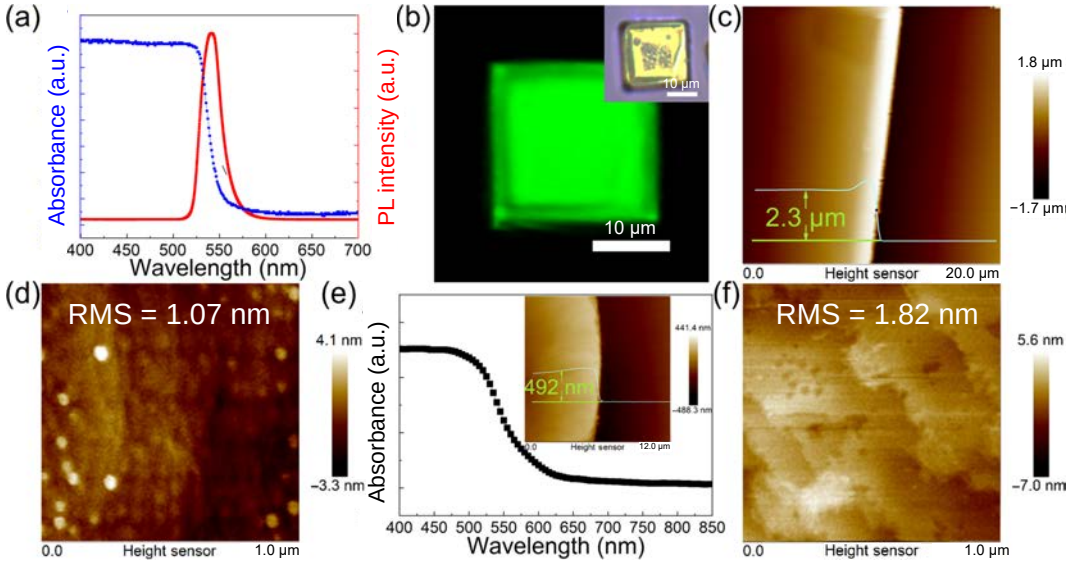

Figure 3 (a) Absorption and PL spectra, (b) PL mapping and the corresponding optical photograph, (c) large-area AFM image, and (d) high-resolution AFM image of the $CsPbBr_3$ MCs. (e) Absorption spectrum (inset shows the large-area AFM image) and (f) high-resolution AFM image of the $Cs_3Sb_2I_9$ MCs.

energy of 2.31 eV can be determined. The PL peak is positioned at 543 nm, whereas the sharp peak indicates the good crystallinity of the MCs. Furthermore, as presented in Fig. 3(b), PL mapping of one typical $CsPbBr_3$ MC is as well performed, where the inset shows the corresponding optical image. It is obvious that there is strong PL emission occurred from the cubic $CsPbBr_3$ MC, with the stronger intensity coming from the inner region of the MC as compared with that of the edge region. This spatial intensity variation can be attributed to the morphology, the relatively low specific surface area and the low surface defect density of the MCs [32]. Based on the atomic force microscope (AFM) measurement, the thickness and the root-mean-square (RMS) surface roughness of a typical $CsPbBr_3$ MC are determined to be ~ 2.3 μm (Fig. 3(c)) and ~ 1.07 nm (Fig. 3(d)), respectively, suggesting a fairly smooth surface morphology. At the same time, the XRD pattern of the $CsPbBr_3$ film fabricated by conventional spin coating was also collected (Fig. S3 in the ESM), revealing that the pure cubic $CsPbBr_3$ film is obtained. The sharp UV–vis absorption edge and the strong PL peak as well suggest the good crystallinity and a direct bandgap of 2.38 eV of the spin-coated film (Fig. S4 in the ESM). As expected, the corresponding SEM image shows the formation of a compact film with crystalline grains and without any noticeable pinholes (Fig. S5 in the ESM), attributed to the combination of anti-solvent characteristics in spin-coating and grain growth in subsequent high-temperature annealing. All these results can clearly demonstrate the comparable film quality between our drop-casted $CsPbBr_3$ MCs and the spin-coated films, even though the drop-casting method involves the simpler fabrication procedure and the lower process temperature.

In addition, the UV–vis absorption spectrum of the $Cs_3Sb_2I_9$ MCs is also shown in Fig. 3(e). One can see that the absorption edge is located at 588 nm, from which a bandgap energy of 2.10 eV can be determined. AFM was as well used to assess the thickness and surface morphology of the MCs. As shown in the inset of Figs. 3(e) and 3(f), the typical thickness and the RMS surface roughness of the MC are ~ 492 and ~ 1.82 nm, respectively, suggesting its smooth surface morphology. In addition, the XRD pattern of the $Cs_3Sb_2I_9$ film fabricated by spin coating is also depicted in Fig. S6 in the ESM. It is clear that there are two obvious peaks witnessed for the L-$Cs_3Sb_2I_9$ phase (i.e.,

(201) plane with I(f) = 86.0 from PDF#88–0690) and the D-$Cs_3Sb_2I_9$ phase (i.e., (203) plane with I(f) = 100.0 from PDF#88–0689), illustrating the existence of the mixed phases of the spin-coated film. The bandgap of 2.38 eV can be calculated from the UV–vis absorption spectrum of the $Cs_3Sb_2I_9$ film (Fig. S7 in the ESM). Based on the SEM image of the $Cs_3Sb_2I_9$ film, shallow gullies are appeared on the smooth surface (Fig. S8 in the ESM), which can be caused by the evaporation of SbI_3 during the annealing step [28]. Impressively, the drop-casting method is capable of producing the high-quality phase-pure L-$Cs_3Sb_2I_9$ MCs with the modest fabrication procedure and without any high-temperature annealing. To confirm that this low-temperature annealing is sufficient to make the solvent evaporate completely, thermogravimetric analysis (TGA) of the $CsPbBr_3$ and L-$Cs_3Sb_2I_9$ MCs was also measured, as shown in Fig. S9 in the ESM. It is seen that for the $CsPbBr_3$ MCs, the weight ratio remains 99% even the temperature is heated to 250 °C, which indicates the annealing process is enough for $CsPbBr_3$. As for $Cs_3Sb_2I_9$, the weight ratio even maintains 100% at 250 °C, suggesting that 70 °C can remove almost all the residual solvents.

In order to assess the photoelectric performance of the fabricated materials, the $CsPbBr_3$ MCs were then configured into photodetectors and carefully characterized. The schematic of the device structure used in this work is depicted in Fig. S10 in the ESM. The photocurrent–voltage (I–V) curves collected under different light intensities are shown in Fig. S11 in the ESM. All the I–V curves are linear, suggesting the nearly ohmic contact properties between MCs and Au electrodes, which is beneficial for the collection of photogenerated carriers. Figure 4(a) gives the current–time (I–t) curves of the MCs and the spin-coated film-based photodetectors under chopped illumination with an intensity of 450 mW/cm^2. They both show the stable switching on/off behavior, where the photocurrent of MCs is about 13 times larger than that of the spin-coated film device. The on/off current ratio of the MCs-based photodetector is calculated to be 5.5×10^3. These photocurrents under different light intensities are also shown in Fig. 4(b). One can see that the photocurrents of both MCs and spin-coated film devices show a linear relationship with the light intensities. In general, the linear dynamic range (LDR), representing the linear light intensity of response range for a photodetector, can be calculated according to the expression of $\mathrm{LDR} = 20\log\frac{P_{\mathrm{upper}}}{P_{\mathrm{lower}}}$, where P_{upper} is the maximum light intensity limit within the linearity, and P_{lower} is the minimum light intensity [33, 34]. In this case, the LDR of the MCs-based photodetector is determined to be as large as 82.6 dB. Since the values of P_{upper} and P_{lower} are limited to the equipment employed here, together with the good linearity of photocurrents with light intensities, the actual LDR value can be even larger than 82.6 dB. Besides, the responsivities (R) of the photodetectors are compiled and displayed in Fig. 4(c), in which R can be calculated through the equation of $R = \frac{I_p}{\Phi S}$, where I_p, Φ, and S are the photocurrent, the light intensity, and the active area of the photodetector, respectively. In specific, it is obvious that R keeps increasing with the decreasing light intensity, which is a common character of the photodetectors. Another two important performance parameters of photodetectors, the detectivity (D^*) and external quantum efficiency (EQE), can be defined as $D^* = RS^{1/2}/(2eI_{\mathrm{dark}})^{1/2}$ and EQE = $hcR/e\lambda$ (e, I_{dark}, h, c, and λ represent the electronic charge, the dark current, the Planck's constant, the velocity of the incident light, and the wavelength of the incident light, respectively) [35]. As shown in Fig. S12 in the ESM, the D^* and EQE of the photodetectors are calculated according to the equations described above. Not surprisingly, the EQE of the $CsPbBr_3$ MCs is found to be much larger than that of the spin-coated film, where the largest EQE arrives at 2,758%. However, one can see that the D^* of the film is comparable to that of the MCs, which is ascribed to its relatively low dark current. Moreover, the response speed is also an essential parameter for the performance evaluation of photodetectors, especially for high-frequency devices. As presented in Fig. 4(d), the high-resolution I–t curves of the $CsPbBr_3$ MCs and film based photodetectors are measured, where the rise time is defined as the time required for current to increase from 10% to 90% of its peak value, and similarly, the decay time is from 90% to 10% of the peak value. The rise and decay times of the $CsPbBr_3$ MCs-based photodetectors are then determined to be as fast as 153 and 152 μs, but the film-based ones are only 362 and 538 μs, accordingly, indicating the superior device performance of the drop-casted MCs.

Then the $Cs_3Sb_2I_9$ MCs and spin-coated films are also constructed into photodetectors to examine their photoelectric performance. The I–V curves of the photodetectors under illumination with different light intensities are shown in Fig. S13

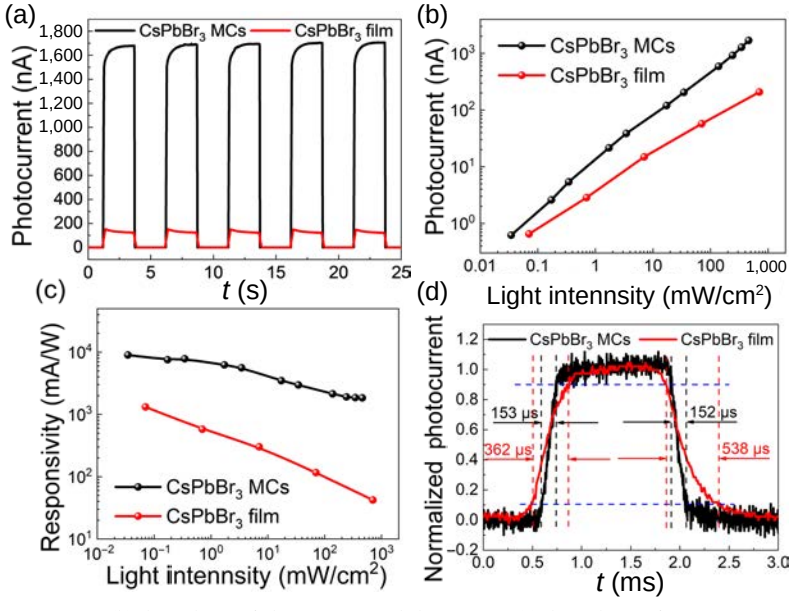

Figure 4 (a) Time-dependent photoresponse, (b) dependence of photocurrent on light intensity, (c) dependence of responsivity on the light intensity, and (d) high-resolution current vs. time curve for the $CsPbBr_3$ MCs and film.

in the ESM. The linear relationship of the *I*–*V* curves indicates the nearly ohmic contact properties between MCs and Au electrodes, which is essential for the effective collection of photogenerated carriers. Figure 5(a) gives the *I*–*t* curves of the MCs and spin-coated film-based photodetectors under chopped illumination with an intensity of 730 mW/cm^2. They both show the repeatable switching on/off characteristics, where the photocurrent of MCs is more than five times larger than that of the film. The on/off current ratio of the MCs-based photodetector is calculated to be 105. The photocurrents under illumination with different light intensities are depicted in Fig. 5(b). The photocurrents of both the MCs and the film show a linear relationship with light intensities, while a broad LDR of larger than 80 dB is also acquired. Moreover, the responsivities of both photodetectors are also shown in Fig. 5(c). It is clear that *R* keeps increasing with the decreasing light intensity, which can be found in most photodetectors reported. The *D** and EQE of the photodetectors are as well calculated and presented in Fig. S14 in the ESM. Similar to the responsivity, the *D** and EQE of the $Cs_3Sb_2I_9$ MCs are much larger than those of the films. One can see that the largest EQE of the $Cs_3Sb_2I_9$ MCs is ~ 123%, whereas the *D** is as high as 1.27×10^{11} Jones. In addition, the response speed of the $Cs_3Sb_2I_9$ MCs-based photodetector was also determined through the high-resolution *I*–*t* curve shown in Fig. 5(d). The rise and decay times are as short as 149 and 158 μs, respectively. However, as depicted in Fig. S15 in the ESM the response speed of the $Cs_3Sb_2I_9$ film-based photodetector can only reach 3.9 and 5.2 ms, respectively. The performance parameters of the AIHPs photodetectors reported recently are then compiled in Table 1 and compared with the MCs devices developed in our work. Evidently, the high responsivity and rapid response speed of the MCs photodetectors fabricated by the simple low-temperature drop-casting method are superior to those obtained by spin-coating, chemical vapour deposition (CVD), or co-evaporation techniques, which can be ascribed to the good crystal quality of the drop-casted MCs. Besides, the moisture stability of the $CsPbBr_3$ and $Cs_3Sb_2I_9$ MCs was as well evaluated. As shown in Fig. S16 in the ESM, the MCs were stored in an ambient environment with the humidity of 70% for one month, and then the UV–vis absorption spectra were re-measured, compared against the pristine ones. One can observe that the absorption edges of the MCs maintain the same without any noticeable degradation, indicating their excellent stability.

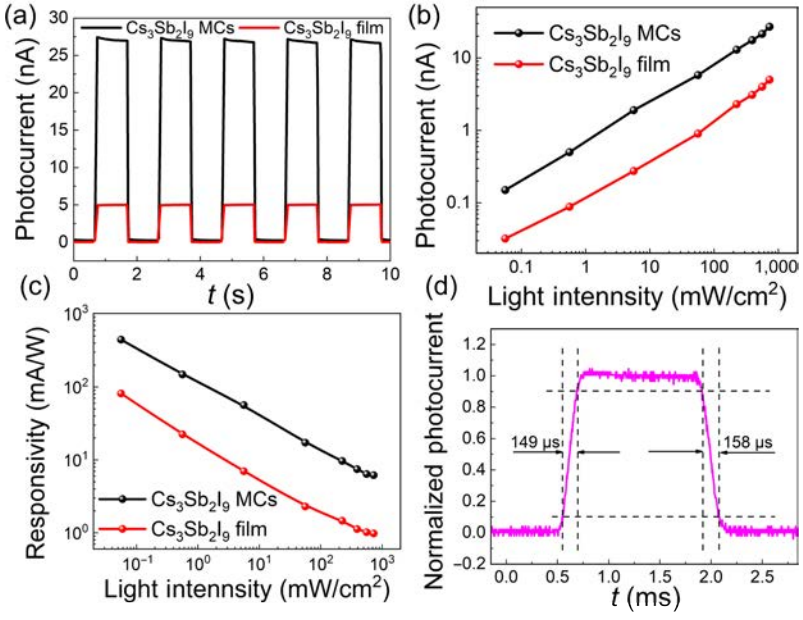

Figure 5 (a) Time-dependent photoresponse, (b) dependence of photocurrent on the light intensity, and (c) dependence of responsivity on the light intensity illuminated on the $Cs_3Sb_2I_9$ MCs and the counterpart film. (d) High-resolution current versus time curve for the $Cs_3Sb_2I_9$ MCs.

Table 1 Comparison of various figure of merits of AIHPs-based photodetectors

Halides	Method/morphology	*R* (mA/W)	*D**(Jones)	Rise/decay time (ms)	References
$Cs_3Sb_2Br_9$	Solution/single crystal	3,800	2.6×10^{12}	24/48	[26]
$Cs_3Sb_2I_9$	CVD/nanoplate	40	1.26×10^{11}	0.096/0.058	[32]
$Cs_3Bi_2I_9$	Solution/single crystal	7.2	10^{11}	0.247/0.23	[36]
$Cs_3Cu_2I_5$	Solution/thin film	64.9	6.9×10^{11}	26.2/49.9	[37]
PEDOT:PSS/$Cs_3Bi_2I_6Br_3$/C_{60}/BCP	Solution/thin film	16	4.6×10^{11}	40.7/27.1	[38]
GaN/$CsPbBr_3$ MCs/n-ZnO	CVD/MCs	89.5	10^{14}	0.1/0.14	[39]
$CsPbBr_3$	CVD/microplatelets	1,330	8.6×10^{11}	20.9/24.6	[40]
$CsPbBr_3$	Co-evaporation/microwires	7,660	4.05×10^{12}	275/550	[41]
$CsPbI_2Br$	Solution/thin film	12	10^{11}	0.175/0.180	[42]
$CsPbIBr_2$	Solution/thin film	8	10^{11}	0.320/0.230	[42]
$CsPbI_3$-$CsPbBr_3$	Solution/nanowire array	125	N/A	0.7/0.8	[43]
$CsPbBr_3$	Solution/MCs	8,990	1.52×10^{12}	0.153/0.152	This work
$Cs_3Sb_2I_9$	Solution/MCs	446	1.27×10^{11}	0.149/0.158	This work

3 Conclusions

In conclusion, cubic $CsPbBr_3$ and L-$Cs_3Sb_2I_9$ MCs with high crystal quality have been fabricated by the solution-processed low-temperature drop-casting method. Their counterpart films have also been fabricated by the conventional spin-coating technique. Both the MCs and spin-coated films are configured into photodetectors, where their photodetection performance was studied and compared in detail. The MCs-based photodetectors are found to exhibit much higher performance than that of the spin-coated films' devices. The responsivity of the $CsPbBr_3$ MCs is as large as 8,990 mA/W, which is more than 13 times larger than that of their films. Besides, the responsivity $Cs_3Sb_2I_9$ MCs is also determined to be as large as 446 mA/W, while that of the films is only 81 mA/W. The superior performance of the MCs can be attributed to their high crystal quality and phase purity contributed by the drop-casting method. Our work illustrates the simple low-temperature and solution processing manufacturing to achieve high-quality phase-pure AIHPs MCs, which will further the development of AIHPs-based optoelectronic devices.

4 Experimental section

4.1 Perovskite precursor synthesis

For the $CsPbBr_3$ solution, 0.48 mmol CsBr and 0.48 mmol $PbBr_2$ were dissolved in 1 mL of dimethylsulfoxide. For the $Cs_3Sb_2I_9$ solution, 1 mmol of CsI and 0.67 mmol of SbI_3 were dissolved in 1 mL of dimethylformamide (DMF). The solutions were then stirred at room temperature overnight.

4.2 Materials and device fabrication

All the materials were fabricated in a nitrogen-filled glovebox, where the oxygen and moisture concentration were well controlled at the ppm level. The glass substrates were ultrasonically washed by acetone, ethanol, and deionized (DI) water in succession for 15 min first. Then these substrates were treated with mild oxygen plasma to improve the hydrophilia. For the drop-casting method, 5 μL of $CsPbBr_3$ or $Cs_3Sb_2I_9$ solution was dripped on the substrate, followed by thermal annealing at 120 or 70 °C for 5 min. For the spin-coating method, 30 μL of $CsPbBr_3$ or $Cs_3Sb_2I_9$ solution was spin-coated onto the substrate at 3,000 rpm for 40 s, followed by thermal annealing at 250 or 100 °C for 10 min. For the fabrication of the photodetectors, 50-nm-thick Au electrodes were thermally evaporated onto the samples with the assistance of shadow masks, where the channel length and width were 10 and 70 μm, respectively.

4.3 Film and device characterization

XRD (D2 phaser with Cu Kα radiation, Bruker) was used to evaluate the crystal structure of the obtained MCs and films. The morphologies of the MCs and films were characterized with SEM (FEI quanta 450 FEG SEM). The thickness and the surface roughness of the MCs were characterized by AFM (Bruker dimension icon AFM). UV–vis absorption spectra were recorded using a Hitachi UH4150 UV–vis–NIR spectrophotometer (the MCs can be directly used for the measurement of the absorption spectra thanks to their dense distribution. In this case, using another glass substrate as a reference, a perfect absorption spectrum of the MCs can be easily acquired). The PL spectrum was acquired by a Hitachi F-4600 spectrophotometer and the wavelength of the excitation light is set at 370 nm. The PL mapping was recorded by WITec RAMAN alpha 300R system with the wavelength of the excitation laser fixed at 532 nm. TGA curves were measured by SDT Q600 at a heating rate of 5 °C/min in a nitrogen atmosphere. The electrical performance of fabricated devices was characterized by a standard electrical probe station and an Agilent 4155C semiconductor analyzer (Agilent technologies, California, USA). Lasers with a wavelength of 450 nm were used as the light sources for the photodetector measurement, while the power of the incident irradiation was measured using a power meter (PM400, thorlabs). An attenuator was also employed to tune the irradiation power illuminating on the device. For determining the response time of the detector, a low-noise current amplifier (SR570, Stanford Research Systems, USA) combined with a digital oscillator (TBS 1102B EDU, Tektronix, USA) was used to obtain high-resolution current-time curves.

Acknowledgements

We acknowledge the General Research Fund (No. CityU 11306520) and the Theme based Research (No. T42-103/16-N) of the Research Grants Council of Hong Kong, China, and the Foshan Innovative and Entrepreneurial Research Team Program (No. 2018IT100031).

Electronic Supplementary Material: Supplementary material (further details of the SEM image of the $CsPbBr_3$ MCs, SEM image of the $Cs_3Sb_2I_9$ MCs, XRD pattern of the $CsPbBr_3$ film, absorption and PL spectra of the $CsPbBr_3$ film, SEM image of the $CsPbBr_3$ film, XRD pattern of the $Cs_3Sb_2I_9$ film, the absorption spectrum of the $Cs_3Sb_2I_9$ film, SEM image of the $Cs_3Sb_2I_9$ film, TGA of the $CsPbBr_3$ and $Cs_3Sb_2I_9$ MCs, schematic of the device structure, *I*–*V* curves of the $CsPbBr_3$ MCs, EQE, and detectivity of the $CsPbBr_3$ MCs and films, *I*–*V* curves of the $Cs_3Sb_2I_9$ MCs, EQE, and detectivity of the $Cs_3Sb_2I_9$ MCs and films, high-resolution *I*–*t* curve for the $Cs_3Sb_2I_9$ film, UV–vis spectra of the $CsPbBr_3$ and $Cs_3Sb_2I_9$ MCs after stored in the ambient environment) is available in the online version of this article at https://doi.org/10.1007/s12274-021-3907-9.

References

[1] Hu, J.; Oswald, I. W. H.; Stuard, S. J.; Nahid, M. M.; Zhou, N. H.; Williams, O. F.; Guo, Z. K.; Yan, L.; Hu, H. M.; Chen, Z. et al. Synthetic control over orientational degeneracy of spacer cations enhances solar cell efficiency in two-dimensional perovskites. *Nat. Commun.* **2019**, *10*, 1276.

[2] Xiong, J.; Dai, Z. J.; Zhan, S. P.; Zhang, X. W.; Xue, X. G.; Liu, W. Z.; Zhang, Z. L.; Huang, Y.; Dai, Q. L.; Zhang, J. Multifunctional passivation strategy based on tetraoctylammonium bromide for efficient inverted perovskite solar cells. *Nano Energy* **2021**, *84*, 105882.

[3] Kim, Y. H.; Kim, S.; Kakekhani, A.; Park, J.; Park, J.; Lee, Y. H.; Xu, H. X.; Nagane, S.; Wexler, R. B.; Kim, D. H. et al. Comprehensive defect suppression in perovskite nanocrystals for high-efficiency light-emitting diodes. *Nat. Photonics* **2021**, *15*, 148–155.

[4] Sun, B.; Xu, Y.; Chen, Y. H.; Huang, W. Two-dimensional ruddlesden-popper layered perovskite for light-emitting diodes. *APL Mater.* **2020**, *8*, 040901.

[5] Zhu, T.; Yang, Y. R.; Zheng, L. Y.; Liu, L.; Becker, M. L.; Gong, X. Solution-processed flexible broadband photodetectors with solution-processed transparent polymeric electrode. *Adv. Funct. Mater.* **2020**, *30*, 1909487.

[6] Lai, Z. X.; Meng, Y.; Zhu, Q.; Wang, F.; Bu, X. M.; Li, F. Z.; Wang, W.; Liu, C. T.; Wang, F.; Ho, J. C. High-performance flexible self-powered photodetectors utilizing spontaneous electron and hole separation in quasi-2D halide perovskites. *Small* **2021**, *17*, 2100442.

[7] Burschka, J.; Pellet, N.; Moon, S. J.; Humphry-Baker, R.; Gao, P.; Nazeeruddin, M. K.; Grätzel, M. Sequential deposition as a route to high-performance perovskite-sensitized solar cells. *Nature* **2013**, *499*, 316–319.

[8] Xing, G. C.; Wu, B.; Wu, X. Y.; Li, M. J.; Du, B.; Wei, Q.; Guo, J.; Yeow, E. K. L.; Sum, T. C.; Huang, W. Transcending the slow bimolecular recombination in lead-halide perovskites for electroluminescence. *Nat. Commun.* **2017**, *8*, 14558.

[9] Guo, J.; Liu, T. H.; Li, M. J.; Liang, C.; Wang, K. Y.; Hong, G.; Tang, Y. X.; Long, G. K.; Yu, S. F.; Lee, T. W. et al. Ultrashort laser pulse doubling by metal-halide perovskite multiple quantum wells. *Nat. Commun.* **2020**, *11*, 3361.

[10] Ali, N.; Rauf, S.; Kong, W.; Ali, S.; Wang, X. Y.; Khesro, A.; Yang, C. P.; Zhu, B.; Wu, H. Z. An overview of the decompositions in organo-metal halide perovskites and shielding with 2-dimensional perovskites. *Renew. Sustain. Energy Rev.* **2019**, *109*, 160–186.

[11] Wang, Q.; Ma, M.; Cui, K.; Li, Y.; Wu, X. H. Investigation of electronic band and moisture stability of 2D hybrid perovskite crystals with ethanolamine organic layer. *J. Alloys Compd.* **2021**, *854*, 157187.

[12] Fu, Q. X.; Tang, X. L.; Huang, B.; Hu, T.; Tan, L. C.; Chen, L.; Chen, Y. W. Recent progress on the long-term stability of perovskite solar cells. *Adv. Sci.* **2018**, *5*, 1700387.

[13] Vasileiadou, E. S.; Wang, B.; Spanopoulos, I.; Hadar, I.; Navrotsky, A.; Kanatzidis, M. G. Insight on the stability of thick layers in 2D ruddlesden-popper and dion-jacobson lead iodide perovskites. *J. Am. Chem. Soc.* **2021**, *6*, 2523–2536.

[14] Stoumpos, C. C.; Malliakas, C. D.; Kanatzidis, M. G. Semiconducting tin and lead iodide perovskites with organic cations: Phase transitions, high mobilities, and near-infrared photoluminescent properties. *Inorg. Chem.* **2013**, *52*, 9019–9038.

[15] Li, Z. Z.; Zhou, F. G.; Wang, Q.; Ding, L. M.; Jin, Z. W. Approaches for thermodynamically stabilized $CsPbI_3$ solar cells. *Nano Energy* **2020**, *71*, 104634.

[16] Zhong, Y. G.; Liao, K.; Du, W. N.; Zhu, J. R.; Shang, Q. Y.; Zhou, F.; Wu, X. X.; Sui, X. Y.; Shi, J. W.; Yue, S. et al. Large-scale thin $CsPbBr_3$ single-crystal film grown on sapphire via chemical vapor deposition: Toward laser array application. *ACS Nano* **2020**, *14*, 15605–15615.

[17] Hendriks, K. H.; van Franeker, J. J.; Bruijnaers, B. J.; Anta, J. A.; Wienk, M. M.; Janssen, R. A. J. 2-Methoxyethanol as a new solvent for processing methylammonium lead halide perovskite solar cells. *J. Mater. Chem. A* **2017**, *5*, 2346–2354.

[18] Zhang, C. Q.; Wang, K.; Wang, Y. L.; Subhani, W. S.; Jiang, X.; Wang, S. M.; Bao, H. X.; Liu, L.; Wan, L.; Liu, S. Z. Low-temperature crystallization of $CsPbIBr_2$ perovskite for high performance solar cells. *Sol. RRL* **2020**, *4*, 2000254.

[19] Zeng, J. P.; Li, X. M.; Wu, Y.; Yang, D. D.; Sun, Z. G.; Song, Z. H.; Wang, H.; Zeng, H. B. Space-confined growth of $CsPbBr_3$ film achieving photodetectors with high performance in all figures of merit. *Adv. Funct. Mater.* **2018**, *28*, 1804394.

[20] Huang, D. W.; Xie, P. F.; Pan, Z. X.; Rao, H. S.; Zhong, X. H. One-step solution deposition of $CsPbBr_3$ based on precursor engineering for efficient all-inorganic perovskite solar cells. *J. Mater. Chem. A* **2019**, *7*, 22420–22428.

[21] Fan, Q. Q.; Biesold-McGee, G. V.; Ma, J. Z.; Xu, Q. N.; Pan, S.; Peng, J.; Lin, Z. Q. Lead-free halide perovskite nanocrystals: Crystal structures, synthesis, stabilities, and optical properties. *Angew. Chem., Int. Ed.* **2020**, *59*, 1030–1046.

[22] Ghosh, S.; Pradhan, B. Lead-free metal halide perovskite nanocrystals: Challenges, applications, and future aspects. *ChemNanoMat* **2019**, *5*, 300–312.

[23] Yao, H. H.; Zhou, F. G.; Li, Z. Z.; Ci, Z. P.; Ding, L. M.; Jin, Z. W. Strategies for improving the stability of tin-based perovskite ($ASnX_3$) solar cells. *Adv. Sci.* **2020**, *7*, 1903540.

[24] Marshall, K. P.; Walker, M.; Walton, R. I.; Hatton, R. A. Enhanced stability and efficiency in hole-transport-layer-free $CsSnI_3$ perovskite photovoltaics. *Nat. Energy* **2016**, *1*, 16178.

[25] Park, B. W.; Philippe, B.; Zhang, X. L.; Rensmo, H.; Boschloo, G.; Johansson, E. M. J. Bismuth based hybrid perovskites $A_3Bi_2I_9$ (A: Methylammonium or cesium) for solar cell application. *Adv. Mater.* **2015**, *27*, 6806–6813.

[26] Zheng, Z.; Hu, Q. S.; Zhou, H. Z.; Luo, P.; Nie, A. M.; Zhu, H. M.; Gan, L.; Zhuge, F. W.; Ma, Y.; Song, H. S. et al. Submillimeter and lead-free $Cs_3Sb_2Br_9$ perovskite nanoflakes: Inverse temperature crystallization growth and application for ultrasensitive photodetectors. *Nanoscale Horiz.* **2019**, *4*, 1372–1379.

[27] Szklarz, P.; Jakubas, R.; Gągor, A.; Bator, G.; Cichos, J.; Karbowiak, M. $[NH_2CHNH_2]_3Sb_2I_9$: A lead-free and low-toxicity organic-inorganic hybrid ferroelectric based on antimony (III) as a potential semiconducting absorber. *Inorg. Chem. Front.* **2020**, *7*, 1780–1789.

[28] Saparov, B.; Hong, F.; Sun, J. P.; Duan, H. S.; Meng, W. W.; Cameron, S.; Hill, I. G.; Yan, Y. F.; Mitzi, D. B. Thin-film preparation and characterization of $Cs_3Sb_2I_9$: A lead-free layered perovskite semiconductor. *Chem. Mater.* **2015**, *27*, 5622–5632.

[29] Singh, A.; Boopathi, K. M.; Mohapatra, A.; Chen, Y. F.; Li, G.; Chu, C. W. Photovoltaic performance of vapor-assisted solution-processed layer polymorph of $Cs_3Sb_2I_9$. *ACS Appl. Mater. Interfaces* **2018**, *10*, 2566–2573.

[30] Chonamada, T. D.; Dey, A. B.; Santra, P. K. Degradation studies of $Cs_3Sb_2I_9$: A lead-free perovskite. *ACS Appl. Energy Mater.* **2020**, *3*, 47–55.

[31] Zhou, H.; Zeng, J. P.; Song, Z. N.; Grice, C. R.; Chen, C.; Song, Z. H.; Zhao, D. W.; Wang, H.; Yan, Y. F. Self-powered all-inorganic perovskite microcrystal photodetectors with high detectivity. *J. Phys. Chem. Lett.* **2018**, *9*, 2043–2048.

[32] Shil, S. K.; Wang, F.; Lai, Z. X.; Meng, Y.; Wang, Y. P.; Zhao, D. X.; Hossain, M. K.; Egbo, K. O.; Wang, Y.; Yu, K. M. et al. Crystalline all-inorganic lead-free $Cs_3Sb_2I_9$ perovskite microplates with ultra-fast photoconductive response and robust thermal stability. *Nano Res*. **2014**, *14*, 4116−4124.

[33] Zhang, Y. X.; Liu, Y. C.; Xu, Z.; Yang, Z.; Liu, S. Z. 2D perovskite single crystals with suppressed ion migration for high-performance planar-type photodetectors. *Small* **2020**, *16*, 2003145.

[34] Liu, Y. C.; Ye, H. C.; Zhang, Y. X.; Zhao, K.; Yang, Z.; Yuan, Y. B.; Wu, H. D.; Zhao, G. T.; Yang, Z. P.; Tang, J. et al. Surface-tension-controlled crystallization for high-quality 2D perovskite single crystals for ultrahigh photodetection. *Matter* **2019**, *1*, 465–480.

[35] Meng, Y.; Lan, C. Y.; Li, F. Z.; Yip, S.; Wei, R. J.; Kang, X. L.; Bu, X. M.; Dong, R. T.; Zhang, H.; Ho, J. C. Direct vapor-liquid-solid synthesis of all-inorganic perovskite nanowires for high-performance electronics and optoelectronics. *ACS Nano* **2019**, *13*, 6060–6070.

[36] Li, W. G.; Wang, X. D.; Liao, J. F.; Jiang, Y.; Kuang, D. B. Enhanced on-off ratio photodetectors based on lead-free $Cs_3Bi_2I_9$ single crystal thin films. *Adv. Funct. Mater.* **2020**, *30*, 1909701.

[37] Zhang, Z. X.; Li, C.; Lu, Y.; Tong, X. W.; Liang, F. X.; Zhao, X. Y.; Wu, D.; Xie, C.; Luo, L. B. Sensitive deep ultraviolet photodetector and image sensor composed of inorganic lead-free $Cs_3Cu_2I_5$ perovskite with wide bandgap. *J. Phys. Chem. Lett.* **2019**, *10*, 5343–5350.

[38] Liu, D.; Yu, B. B.; Liao, M.; Jin, Z. X.; Zhou, L.; Zhang, X. X.; Wang, F. Y.; He, H. T.; Gatti, T.; He, Z. B. Self-powered and broadband lead-free inorganic perovskite photodetector with high stability. *ACS Appl. Mater. Interfaces* **2020**, *12*, 30530–30537.

[39] Tian, C. C.; Wang, F.; Wang, Y. P.; Yang, Z.; Chen, X. J.; Mei, J. J.; Liu, H. Z.; Zhao, D. X. Chemical vapor deposition method grown all-inorganic perovskite microcrystals for self-powered photodetectors. *ACS Appl. Mater. Interfaces* **2019**, *11*, 15804–15812.

[40] Li, Y.; Shi, Z. F.; Lei, L. Z.; Zhang, F.; Ma, Z. Z.; Wu, D.; Xu, T. T.; Tian, Y. T.; Zhang, Y. T.; Du, G. T. et al. Highly stable perovskite photodetector based on vapor-processed micrometer-scale $CsPbBr_3$ microplatelets. *Chem. Mater.* **2018**, *30*, 6744–6755.

[41] Tong, G. Q.; Jiang, M. W.; Son, D. Y.; Ono, L. K.; Qi, Y. B. 2D derivative phase induced growth of 3D all inorganic perovskite micro-nanowire array based photodetectors. *Adv. Funct. Mater.* **2020**, *30*, 2002526.

[42] Zhang, T.; Li, S. B. Self-powered all-inorganic perovskite photodetectors with fast response speed. *Nanoscale Res. Lett.* **2021**, *16*, 6.

[43] Wang, M.; Tian, W.; Cao, F. R.; Wang, M.; Li, L. Flexible and self-powered lateral photodetector based on inorganic perovskite $CsPbI_3$-$CsPbBr_3$ heterojunction nanowire array. *Adv. Funct. Mater.* **2020**, *30*, 909771.